

# Application of single-electron effects to fingerprints of chips using image recognition algorithms

T. Tanamoto,<sup>1</sup> Y. Nishi,<sup>1</sup> and K. Ono<sup>2</sup>

<sup>1</sup>Corporate R & D, Toshiba Corporation, Saiwai-ku, Kawasaki 212-8582, Japan<sup>a)</sup>

<sup>2</sup>Advanced Device Laboratory, RIKEN, Wako-shi, Saitama 351-0198, Japan

(Dated: 25 July 2019)

Single-electron effects have been widely investigated as a typical physical phenomenon in nanoelectronics. The single-electron effect caused by trap sites has been observed in many devices. In general, traps are randomly distributed and not controllable; therefore, different current–voltage characteristics are observed through traps even in silicon transistors having the same device parameters (e.g., gate length). This allows us to use single-electron effects as fingerprints of chips. In this study, we analyze the single-electron effect of traps in conventional silicon transistors. At sufficiently low temperatures at which single-electron effects can be observed (in this case, 1.54 K), we show that current–voltage characteristics can be used as fingerprints of chips through image recognition algorithms. Resonant tunneling parts in the Coulomb diagram can also be used supportively to characterize each device in a low-temperature region. These results show that single-electron effects can provide a quantum version of a physically unclonable function (quantum-PUF).

Single-electron tunneling (SET)<sup>1–14</sup> is experimentally observed when electrons are confined in a small space and the number of electrons is countable. Since the 1990s, many studies have used SET to investigate Kondo effects<sup>15,16</sup> and, more recently, quantum computing<sup>17–20</sup>. Single-electron effects are also observed through trap sites in metal-oxide-semiconductor field-effect transistors (MOSFETs). The single-electron effect caused by a trap site is understandable when trap sites are regarded as quantum dots (QDs), that is, a confined region of electrons with discrete energy levels (Fig. 1). When a single QD is weakly coupled to both the source and the drain electrodes and capacitively coupled to the gate electrode, the measurement of the drain current  $I_D$  as a function of source voltage  $V_S$  and gate voltage  $V_G$  reveals a series of diamond-shaped regions where  $I_D$  is strongly suppressed (see Fig.1 caption for measurement set up).

The features of the diamond-shaped regions, called Coulomb diamonds (CDs), indicate the threshold characteristics of SET. The size of the CD measured in  $V_S$  is the energy of Coulomb charging and/or quantum confinement for the dot. When more than two trap sites are coupled to the source and drain electrodes and contribute to SET, the CD shows a more complicated pattern comprising jagged corner lines<sup>21</sup>. Such complicated CD patterns represent the details of single-electron transport in multiple-QD devices<sup>2,6,8,18</sup>.

Because the spatial positions, density, and energy levels of trap sites are not controllable, the features of CDs can differ in devices produced by the same fabrication process. Therefore, one application of single-electron effects is the use of CDs as a “fingerprint” of devices.

In general, the fingerprint of a device can be considered a physically unclonable function (PUF) if it is unique, unclonable, and reliable. Emerging Internet of Things (IoT) technologies require a stable security system to protect users’ personal information. PUFs are considered an important mech-

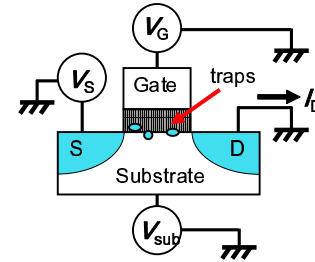


FIG. 1. Schematic of metal-oxide-semiconductor field-effect transistor (MOSFET) channel with three trap sites marked as small circles around the channel region. We measure the current between the source and the drain as we vary the source-drain voltage ( $V_S$ ), gate voltage ( $V_G$ ), and substrate voltage ( $V_{sub}$ ). Trap sites can be treated as quantum dots having discrete energy levels.

anism for providing a unique and inexpensive identification (ID) for each device. A PUF outputs a response ID when a challenge signal is inputted from a server or an authorized system. PUF signals mostly originate from process variations of transistors and circuits. Basic static random access memory (SRAM) consists of two cross-coupled inverters and has fixed memory values only after a 0 or 1 datum is inputted. Therefore, the initial memory value is determined by the threshold variations of the transistors; this is the operating principle of SRAM-PUF<sup>22,23</sup>. The initial defects of memories<sup>24,25</sup> or the circuit delay<sup>26–28</sup> can also be used for generating PUFs.

Roberts *et al.* investigated PUFs using the quantum phenomena of resonant tunneling<sup>29</sup>. Škorić proposed a quantum readout PUF in which a classical PUF is changed by the quantum state of photons<sup>30</sup>. Chen *et al.* proposed a PUF using traps in transistors (trap-PUF), in which the fingerprint of a chip is created by allocating 0 or 1 to each transistor depending on whether the trap site can be detected or not, respectively, in the range of the given voltage region<sup>31</sup>. In the trap-PUF, when a 128-bit ID is requested, at least 128 transistors and related amplifying circuits are needed. The individuality of chips in the trap-PUF is based on the fact that trap distribu-

<sup>a)</sup>Present Address Teikyo University.; Electronic mail: tanamoto@ics.teikyo-u.ac.jp

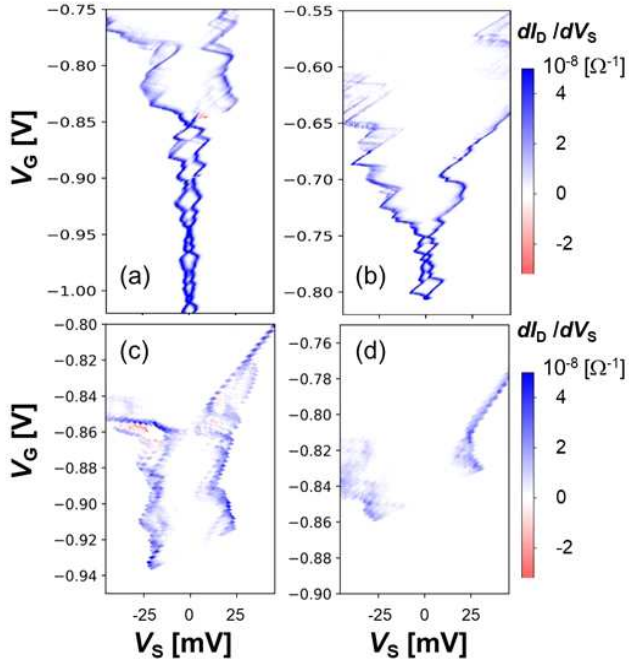


FIG. 2.  $dI_D/dV_S$  (differential conductance) characteristics of trap states in conventional 220-nm-wide transistors. In our measurement,  $|I_D| > 120$  pA is not measured as values saturate in these regions. Thus,  $dI_D/dV_S$  is nominally zero (white color) in these regions.  $dI_D/dV_S$  is calculated from measured current  $I_D$  as a function of source voltage  $V_S$ . The operating temperature in this study is 1.54 K. (a) and (b) show the results for pMOSFETs having the same layout with 125-nm gate length. (c) and (d) show the results for pMOSFETs having the same layout with 125-nm gate length and a silicon oxynitride gate dielectric. Although these two devices have the same layout parameters ( $L$  and  $W$ ), their CDs show different characteristics and can therefore be used to identify each device.

tions cannot be controlled precisely using current fabrication technologies.

In this study, we aim to further extend the use of trap sites in PUFs by using the single-electron effect of traps. We use the features of CDs of traps as fingerprints of devices. When we use single-electron effects as a PUF, one transistor is expected to be sufficient for use as a fingerprint of the whole chip, thereby reducing the trap-PUF circuit area in the chip. We further propose using image-matching algorithms<sup>32</sup> to identify different CDs of transistors. For this purpose, characteristic key points are abstracted by treating CDs as images as in conventional human fingerprint detection. We demonstrate that this approach simplifies the identification process.

We prepared conventional p-type metal-oxide-semiconductor field-effect transistors (pMOSFETs) fabricated on our prototype production line. These pMOSFETs have gate length  $L = 125$ – $145$  nm and fixed gate width  $W = 220$  nm. Coulomb blockade is observed at low temperature, and it disappears as the temperature increases to room temperature. Figure 2 shows examples of the output of  $dI_D/dV_S$  through trap sites in pMOSFETs with  $L = 125$  nm.

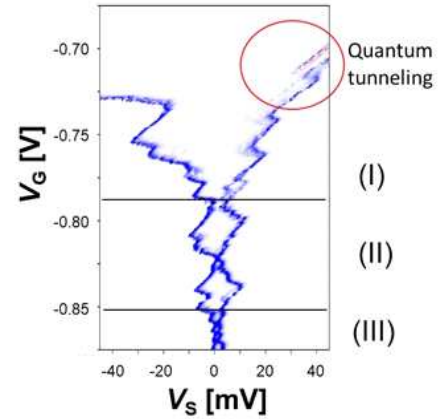


FIG. 3. Most CD images can be separated into three regions based on the physical tunneling mechanism. Region (I): Sub-threshold region. Region (II): Coulomb blockade caused by a couple of traps. Region (III): Coulomb blockade caused by many traps. The blue part shows  $dI_D/dV_S > 0$ . The red part shows  $dI_D/dV_S < 0$  where we consider that resonant tunneling occurs. The quantum tunneling region (resonant tunneling region) is mainly observed in region (I).

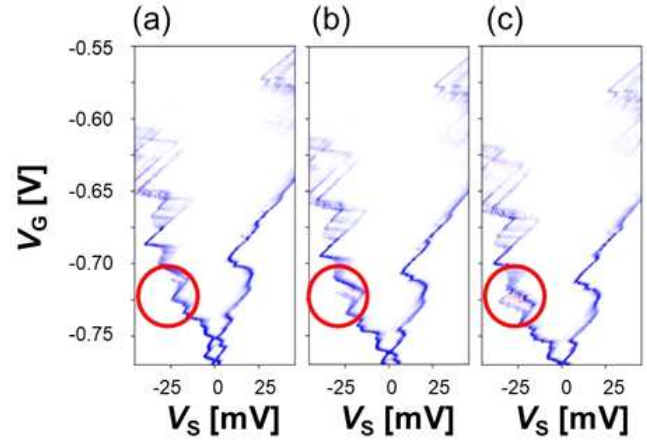


FIG. 4. CD image changes when substrate voltage  $V_{\text{sub}}$  changes. The differential conductance is measured in a conventional pMOSFET with 220-nm width and 125-nm length. (a)  $V_{\text{sub}} = 0.0$  V, (b)  $V_{\text{sub}} = 0.05$  V, and (c)  $V_{\text{sub}} = 0.1$  V. The red circles show an example of a changed part with different  $V_{\text{sub}}$ .

As a reference, the average threshold voltage variations of transistors with  $L = 125$ – $135$  nm are generally calculated in the range of 25–50 mV<sup>33</sup>. Figure 2(a) and (b) show the results for wafers with identical  $L$  and  $W$  that were simultaneously fabricated with the same process conditions. Figure 2(c) and (d) show the results for wafers with identical  $L$  and  $W$  and an additional silicon oxynitride layer in the gate layer but fabricated with different process conditions.

Trap sites, which are often defects, are generally removed to the greatest extent possible because they cause undesirable noises and nonuniformity in device characteristics. These trap

sites are constructed at an atomic level; therefore, their CDs are uncontrollable and unclonable by current CMOS technologies. Thus, even if we fabricate transistors in the same product line, the features of the Coulomb blockade caused by single-electron effects can serve as a unique ID for each device. A CD image is obtained by measuring the current  $I_D$  as a function of gate voltage  $V_G$  and source voltage  $V_S$  and then numerically estimating the differential conductance  $dI_D/dV_S$ .

We divide the experimental data into three regions based on their different physical mechanisms of Coulomb blockade. As seen in Fig. 3, CD images can be divided into three parts depending on the magnitude of the gate bias. Region (I): When  $V_G$  is low, the current flows exponentially as a function of drain voltage. Region (II): When  $V_G$  is applied beyond the subthreshold region, the current increases linearly as a function of  $V_S$ . Region (III): When  $V_G$  is sufficiently large, the current saturates. Regions (I) and (III) correspond to the subthreshold and saturation region of conventional MOSFET operation, respectively. In the subthreshold region, we can see the quantum aspect of the SET. Without quantum effects, the  $I_D$ - $V_S$  characteristics show a step structure. This results from classical Coulomb blockade in which the current is hindered until the applied voltage exceeds the potential at which the next energy level is occupied.

The CD images in Figs. 2 and 3 have many similar jagged corner lines. These features make identification difficult if we compare CD images numerically using conventional data such as  $(V_S, V_G, dI_D/dV_S)$ . In ID applications, unstable output values are not desirable. However, the output signals of devices do not always have identical values. Devices degrade owing to aging effects.

The repetition of measurements between room temperature and low temperature might also change the device condition. Thus, the current-voltage ( $I$ - $V$ ) characteristics will likely change every time the devices are measured. The electronic states of QD devices are generally affected by both  $V_{\text{sub}}$  and  $V_G$  values. A change in  $V_{\text{sub}}$  changes the energy levels of trap sites and the carrier densities of electrodes, resulting in changes in CD images. Therefore, we can emulate the effects of device conditions by changing  $V_{\text{sub}}$ .

Figures 4 show CD images of a pMOSFET with  $L = 135$  nm and  $W = 220$  nm when the substrate bias  $V_{\text{sub}}$  changes from 0.0 to 0.1 V. The details of the CD images clearly change with changes in  $V_{\text{sub}}$ . Two transistors can be distinguished successfully if the two CD images can be distinguished under changes in  $V_{\text{sub}}$ . For example, in the detection of human fingerprints, the surface condition of human fingers changes depending on both internal and external conditions such that human fingers are sometimes wet and sometimes oily. However, fingerprints should be identified every time they are measured. To identify fingerprints, key points in images of fingers are detected and compared with the image stored in the database. Similarly, detecting key points should be effective for finding the similarity of CD images. Although error-correction methods such as fuzzy algorithms can be used for this purpose<sup>37</sup>, we propose a direct method to find the similarity and difference by regarding measurement data as images. Then, experimental data can be compared more flexibly using images in a manner

similar to comparing human fingerprints or pictures.

Many advanced recognition algorithms have been developed for feature detection and image matching over the years<sup>38,39</sup>. Image matching software usually detect three image features: edge, corner, and flat. An edge is a line or border at which a surface terminates, a corner is a place where two converging lines or surfaces meet, and a flat is a surface without any structures or marks. We apply the AKAZE<sup>40</sup>, BRISK<sup>41</sup>, and ORB<sup>42</sup> recognition algorithms to obtain the key points of CD images. The AKAZE<sup>40</sup> algorithm uses a nonlinear diffusion filtering technique whose scale spaces are constructed using a computationally efficient mathematical framework called fast explicit diffusion (FED). ORB<sup>42</sup> is an extended algorithm using other algorithms that is rotation-invariant and noise-resistant. In the BRISK algorithm, key points are detected in octave layers of the image pyramid as well as in in-between layers, and the sampling pattern consists of concentric circles in the neighborhood of each key point. In this study, we used Open Source Computer Vision Library (OpenCV ver.3)<sup>43</sup> based on Python 3. The main advantage of using image matching software is that we can express the difference between two images by a single numerical value called *distance* that is obtained as the output of each algorithm.

Figures 5 show an example of the extraction of characteristic key points between the two CD images of the same device ((a) and (b)) and different devices ((c) and (d)). The connected lines between key points in Figs. 5(a) and (b) look more condensed than those in Figs. 5(c) and (d). To understand the statistical characteristics, it is better to use histograms. Figure 6 shows histograms of the *distances* between the two CD images. The blue and yellow data show the distributions of the same and different devices, respectively, with different  $V_{\text{sub}}$ . The results show that the two devices can be distinguished by calculating the *distance* of two CD images. Each recognition algorithm has its own specific parameters such as a threshold and number of feature points. As long as we chose several sets of parameters, we could not see any prominent improvement for some specific parameter sets. Thus, we used the default parameters of each algorithm. The two peaks in the distributions of the same devices (Figs. 6 (b) and (c)) are considered to originate from some detailed data structure in the same devices; we cannot explain the reason at present. Figure 7 shows histograms of the *distances* between the two CD images for devices with different  $L$ s. The *distances* in devices with the same  $L$ s are clearly smaller than those in devices with different  $L$ s, and we can distinguish device IDs by using the CD images. At present, we could not judge which algorithm is best, and therefore, it is better to use a couple of algorithms.

Single-electron effects include various quantum tunneling processes such as cotunneling<sup>3-5</sup>. Here, we simply investigate quantum effects where  $dI_D/dV_S$  has negative values. This is the result of resonant tunneling effects using the discrete energy levels of trap sites. Because the resonant tunneling region is too small for using the image recognition algorithms, we use histograms over data of negative differential conductance ( $dI_D/dV_S < 0$ ), as shown in Fig. 8. Each figure includes several distributions of the negative differential conductance

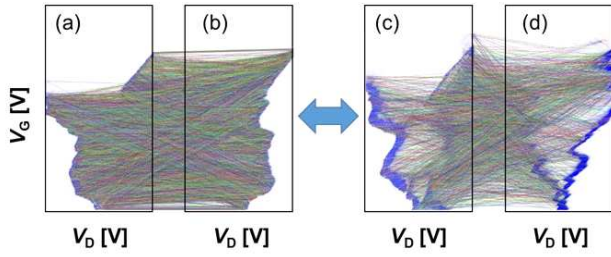


FIG. 5. Examples of extraction of key points from CD images in regions (I) and (II) using AKAZE recognition algorithm. The distance between (a) and (b) is 46.52 ( $V_{sub} = 0.5$  V and 0.6 V) and that between (c) and (d) is 95.40 ( $V_{sub} = 0.1$  V and 0.14 V). pMOSFETs with  $L = 125$  nm.

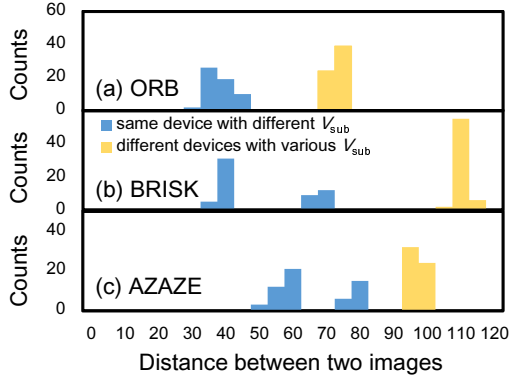


FIG. 6. Comparison of histograms of distances of two images using three recognition algorithms ((a) ORB, (b) BRISK, and (c) AKAZE) for changing  $V_{sub}$ s. The scan region is restricted to 0.15 V. “Same device” shows the results for different  $V_{sub}$ s with the same devices. “Different device” shows the results for different  $V_{sub}$ s with different devices.

with different  $V_{sub}$ s in the range of  $\pm 0.1$  V. The histogram is divided into 50 regions in each of which values of the standard deviation are divided by their average. The calculated deviation resulting from  $V_{sub}$  variations is 0.176% for Fig. 8(a) and 0.385% for Fig. 8(b). The relative difference of the two transistors is calculated by

$$\frac{|\text{Average}(\text{Fig. (a)}) - \text{Average}(\text{Fig. (b)})|}{|\text{Average}(\text{Fig. (a)}) + \text{Average}(\text{Fig. (b)})|/2} = 0.83\%. \quad (1)$$

Thus, the difference is not large. For increased effectiveness, methods such as that discussed in Ref.<sup>29</sup> should be applied. The present method can be applied easily and can be used supportively with the image recognition algorithms. A detailed analysis of resonant tunneling will be conducted in future work.

In this study, CDs are measured at cryogenic temperatures. Note that single-electron effects can be observed even at room temperature if the device is designed appropriately<sup>34–36</sup>. However, this requires additional fabrication processes and incurs higher cost. There is a trade-off between the fabrication cost and the operating temperature. In this study, the number of tested transistors with the same  $L$  and  $W$  is limited because of

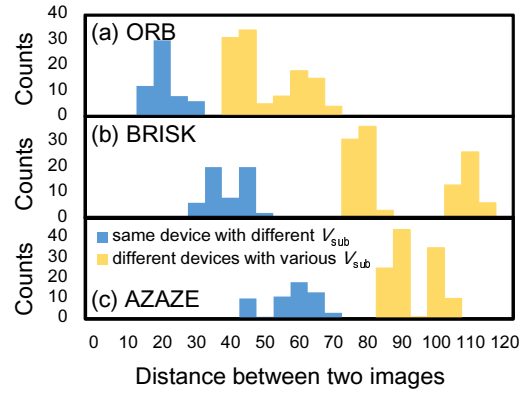


FIG. 7. Comparison of histograms of distances of two images using three recognition algorithms ((a) ORB, (b) BRISK, and (c) AKAZE) for changing  $V_{sub}$ s. Devices with  $L = 125$  nm,  $L = 135$  nm, and  $L = 140$  nm are measured.

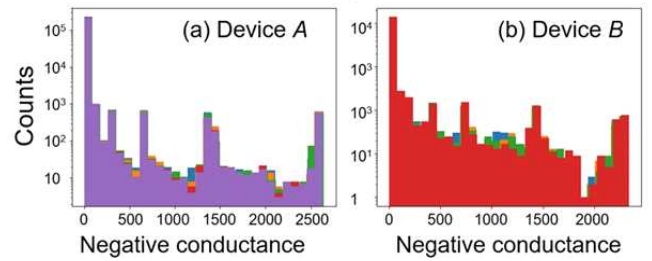


FIG. 8. Histogram of differential conductance  $dI_D/dV_g < 0$  data in two devices A and B with  $L = 125$  nm and  $W = 220$  nm). We can see differences between two devices even if they are made from the same transistors. The different colors corresponds to various  $V_{sub}$ s.

the limited fabrication resources for wafers. The main purpose of this study was to present the concept of a quantum PUF in single-electron devices. An examination of many transistors will be performed in a future study.

In summary, we have proposed a quantum PUF based on single-electron devices. In particular, we showed that we can distinguish two devices by using the distances calculated from CD images. In contrast with the trap-PUF<sup>31</sup> in which many transistors need to be measured, only one transistor is needed to generate the fingerprint of the chip, and thus, the number of devices to be measured is reduced greatly. Note that electrons in traps can be treated as spin-qubits<sup>18</sup>. Because trap distributions differ depending on the transistor, corresponding spin-qubit behaviors are also expected to differ depending on the transistor. Thus, the quantum behavior of an electron in a trap site can also be used as a fingerprint of a chip. This will be explored in a future study.

#### Acknowledgement

TT thanks T. Hiraoka and T. Hioki for useful discussions.

<sup>1</sup>D. V. Averin and K. K. Likharev, in *Mesoscopic Phenomena in Solids*, eds. B. L. Altshuler, P. A. Lee, and R. A. Webb (Elsevier, Amsterdam, 1991)

<sup>2</sup>L. P. Kouwenhoven, C. M. Marcus, P. L. McEuen, S. Tarucha, R. M. Westervelt, and N. S. Wingreen, in *Mesoscopic Electron Transport*, eds. L. L.

- Sohn, G. Schon, L. P. Kowenhoven (Kluwer, Dordrecht, Netherlands, Series E345, 1997).
- <sup>3</sup>D. V. Averin and Yu. V. Nazarov, *Phys. Rev. Lett.* **65**, 2446 (1990).
- <sup>4</sup>L. J. Geerligs, D. V. Averin, and J. E. Mooij, *Phys. Rev. Lett.* **65**, 3037 (1990).
- <sup>5</sup>T. M. Eiles, G. Zimmerli, H. D. Jensen, and J. M. Martinis, *Phys. Rev. Lett.* **69**, 148 (1992).
- <sup>6</sup>H. Sellier, G. P. Lansbergen, J. Caro, S. Rogge, N. Collaert, I. Ferain, M. Jurczak, and S. Biesemans, *Phys. Rev. Lett.* **97**, 206805 (2006).
- <sup>7</sup>Y. Ono, K. Nishiguchi, A. Fujiwara, H. Yamaguchi, H. Inokawa, and Y. Takahashi, *Appl. Phys. Lett.* **90**, 102106 (2007).
- <sup>8</sup>G. P. Lansbergen, R. Rahman, C. J. Wellard, I. Woo, J. Caro, N. Collaert, S. Biesemans, G. Klimeck, L. C. L. Hollenberg, and S. Rogge, *Nat. Phys.* **4**, 656 (2008).
- <sup>9</sup>K. Y. Tan, K. W. Chan, M. Möttönen, A. Morello, C. Yang, J. Donkelaar, A. Alves J.-M. Pirkkalainen, D. N. Jamieson, R. G. Clark, and A. S. Dzurak, *Nano Lett.* **10**, 11 (2010).
- <sup>10</sup>M. Pierre, R. Wacquez, X. Jehl, M. Sanquer, M. Vinet, and O. Cueto, *Nat. Nanotechnol.* **5**, 133 (2010).
- <sup>11</sup>M. F. Gonzalez-Zalba, A. Saraiva, M. J. Calderón, D. Heiss, B. Koiller, and A. J. Ferguson, *Nano Lett.* **14**, 5672 (2014).
- <sup>12</sup>R. Schleser, T. Ihn, E. Ruh, K. Ensslin, M. Tews, D. Pfannkuche, D. C. Driscoll, and A. C. Gossard, *Phys. Rev. Lett.* **94**, 206805 (2005).
- <sup>13</sup>M. Sigrist, T. Ihn, K. Ensslin, M. Reinwald, and W. Wegscheider, *Phys. Rev. Lett.* **98**, 036805 (2007).
- <sup>14</sup>K. Ono, T. Tanamoto, and T. Ohguro, *Appl. Phys. Lett.* **103**, 183107 (2013).
- <sup>15</sup>D. Goldhaber-Gordon, H. Shtrikman, D. Mahalu, D. Abusch-Magder, U. Meirav, and M. A. Kastner, *Nature* **391**, 156 (1998).
- <sup>16</sup>J. Park, A. N. Pasupathy, J. I. Goldsmith, C. Chang, Y. Yaish, J. R. Petta, M. Rinkoski, J. P. Sethna, H. D. Abruña, P. L. McEuen, and D. C. Ralph, *Nature* **417**, 722 (2002).
- <sup>17</sup>J. J. Pla, K. Y. Tan, J. P. Dehollain, W. H. Lim, J. J. L. Morton, D. N. Jamieson, A. S. Dzurak, and A. Morello, *Nature* **489**, 541 (2012).
- <sup>18</sup>K. Ono, G. Giavaras, T. Tanamoto, T. Ohguro, X. Hu, and F. Nori, *Phys. Rev. Lett.* **119**, 156802 (2017).
- <sup>19</sup>T. Tanamoto, Y. Higashi, and J. Deguchi, *J. Appl. Phys.* **124**, 154301 (2018).
- <sup>20</sup>T. Tanamoto, Y. Nishi, and J. Deguchi, *J. Phys. Soc. Jpn.* **88**, 061013 (2019).
- <sup>21</sup>I. M. Ruzin, V. Chandrasekhar, E. I. Levin, and L. I. Glazman, *Phys. Rev. B* **45**, 13469 (1992).
- <sup>22</sup>J. Guajardo, S. S. Kumar, G.-J. Schrijen, and P. Tuyls, *Proc. 9th Int. Workshop on Cryptographic Hardware and Embedded Systems (CHES'07)*, 2007, pp. 63-80.
- <sup>23</sup>D. E. Holcomb, W. P. Burleson, and K. Fu, *IEEE Trans. Comput.* **58**, 1198 (2009).
- <sup>24</sup>T. Marukame, T. Tanamoto, and Y. Mitani, *IEEE Trans. Mag.* **50**, 1 (2014).
- <sup>25</sup>A. Chen, *IEEE Elec. Dev. Lett.* **36**, 138 (2015).
- <sup>26</sup>D. Lim, J. Lee, B. Gassend, G. Suh, M. van Dijk, and S. Devadas, *IEEE Trans. Very Large Scale Integr. (VLSI) Syst.* **13**, 1200 (2005).
- <sup>27</sup>G. E. Suh and S. Devadas, *Proc. 44th Ann. Design Automation Conf. (DAC'07)*, 2007, pp. 9-14.
- <sup>28</sup>T. Tanamoto, S. Yasuda, S. Takaya and S. Fujita, *IEEE Trans. Circuits and Systems II: Express Briefs* **64**, 827-831 (2017).
- <sup>29</sup>J. Roberts, I. E. Bagci, M. A. M. Zawawi, J. Sexton, N. Hulbert, Y. J. Noori, M. P. Young, C. S. Woodhead, M. Missous, M. A. Migliorato, U. Roedig, and R. J. Young, *Sci. Rep.* **5**, 16456 (2015).
- <sup>30</sup>B. Škorić, *Int. J. Quantum Information* **10**, 1250001 (2012).
- <sup>31</sup>J. Chen, T. Tanamoto, H. Noguchi, and Y. Mitani, *2015 IEEE Symp. VLSI Tech.* 2015, pp. 40-41.
- <sup>32</sup>S. J. D. Prince, "Computer Vision: Models, Learning, and Inference" (Cambridge University Press, New York, 2012).
- <sup>33</sup>A. Asenov, *IEEE Trans. Electron Devices* **45**, 2505-2513 (1998).
- <sup>34</sup>K. Uchida, J. Koga, R. Ohba, and A. Toriumi, *IEEE Trans. Electron Devices* **50**, 1623 (2003).
- <sup>35</sup>Y. T. Tan, T. Kamiya, Z. A. K. Durrani, and H. Ahmed, *J. Appl. Phys.* **94**, 633 (2003).
- <sup>36</sup>V. Ray, R. Subramanian, P. Bhadrachalam, L.-C. Ma, C.-U. Kim, and S. J. Koh, *Nature Nanotechnology* **3**, 603 (2008).
- <sup>37</sup>Y. Dodis, R. Ostrovsky, L. Reyzin, and A. Smith, *SIAM Journal on Computing* **38**, 97 (2008).
- <sup>38</sup>Z. Peng, "Efficient matching of robust features for embedded SLAM," Computer Science, University of Stuttgart, 2012.
- <sup>39</sup>S. Isik and K. Ozkan, *International Journal of Applied Mathematics, Electronics and Computers* **3**, 1 (2015).
- <sup>40</sup>P. F. Alcantarilla, J. Nuevo, and A. Bartoli, *Proc. British Machine Vision Conference (BMVC)*, Bristol (2013).
- <sup>41</sup>S. Leutenegger, M. Chli, and R. Siegwart, *Proc. Int. Conf. Computer Vision* 2548 (2011).
- <sup>42</sup>E. Rublee, V. Rabaud, K. Konolige, and G. Bradski, *IEEE International Conference on Computer Vision (ICCV)*, Barcelona, 2564 (2011).
- <sup>43</sup><https://opencv.org/>